applied sciences

MDPI

Article

Photothermal Determination of the Surface Treatment of $Cd_{1-x}Be_xTe$ Mixed Crystals

Jacek Zakrzewski [1,*], Karol Strzałkowski [1,*], Mohammed Boumhamdi [1], Agnieszka Marasek [1], Ali Abouais [1,2] and Daniel M. Kamiński [3]

[1] Institute of Physics, Nicolaus Copernicus University, ul. Grudziadzka 5/7, 87-100 Torun, Poland
[2] Laboratory of Engineering Sciences for Energy, National School of Applied Sciences of El Jadida, BP 1166, El Jadida 24000, Morocco
[3] Institute of Chemical Sciences, Maria Curie-Skłodowska University, pl. Marii Curie-Sklodowskiej 3, 20-031 Lublin, Poland
* Correspondence: jzakrzew@umk.pl (J.Z.); skaroll@umk.pl (K.S.)

Abstract: $Cd_{1-x}Be_xTe$, a new material with potential for X-ray and γ-ray detectors, was analyzed by photothermal piezoelectric spectroscopy. The samples were tested depending on beryllium content and surface preparation. The main aim of the measurements was to extract the energy gap values, which were found for x = 0.01, 0.03, 0.05, and 0.1. It was shown that mechanical (polishing) and chemical (etching) treatment strongly influenced the amplitude and phase spectra of CdBeTe crystals. Piezoelectric spectroscopy allowed for comparing the quality of preparation of both surfaces for a single sample. The sub-surface damaged layer that was created as a result of surface processing had different thermal parameters than the bulk part of the sample. It was responsible for the additional peaks in the amplitude spectrum and changes in the phase spectrum of the photothermal signal. Two different methods of sample etching were analyzed. One completely quenched the signal, and the other did not eliminate the defects present on the surface after the cutting process. The article presents the preliminary interpretation of experimental data using the modified Blonskij model.

Keywords: photothermal spectroscopy; surface defects; semiconductors

Citation: Zakrzewski, J.; Strzałkowski, K.; Boumhamdi, M.; Marasek, A.; Abouais, A.; Kamiński, D.M. Photothermal Determination of the Surface Treatment of $Cd_{1-x}Be_xTe$ Mixed Crystals. *Appl. Sci.* **2023**, *13*, 2113. https://doi.org/10.3390/app13042113

Academic Editors: Li Pei, Jia Shi, Hua Bai, Yunhui Mei and Pingjuan Niu

Received: 22 December 2022
Revised: 31 January 2023
Accepted: 2 February 2023
Published: 7 February 2023

1. Introduction

The quality of the crystals used in the construction of X-ray and gamma radiation detectors affects their efficiency and sensitivity; hence, there is a need to know about their lattice disorder, defects, and both radial and axial homogeneity. Good homogeneity and low defect density lead to significant charge transport properties, low leakage currents, and no conductive short circuits between the detector contacts. The substitution of the native element with a foreign atom within the crystal always leads to undesired effects like disordered structure, defect generation, etc.

Bulk form CdTe and $Cd_{1-x}Zn_xTe$ mixed compounds are applied in X-ray and gamma-ray detectors [1–4], in electrooptic and photorefractive devices [5], and as substrates for epitaxy [6]. $Cd_{1-x}Zn_xTe$ ($0.1 \leq x \leq 0.2$) crystals have been studied intensively over the last twenty years as materials for gamma-ray detection application and also spectroscopic X-ray imaging [7].

Intensive investigations of $Cd_{1-x}Zn_xTe$ have also been carried out in recent years. Lately, C. Zhou et al., studied the extended defects in CdZnTe crystal [8], and the effects of Al-rich AlN transition layers on the performance of CdZnTe films for solar-blind photodetector were investigated by J. Gu [9]. Effects of deep-level traps on the transport properties of high-flux X-ray CdZnTe detectors were investigated by Y. Li et al. [10].

Great attention is also paid to the surface preparation of the samples [11–14]. Surface phenomena play a large role in obtaining crystals in all phases of processing and often affect the parameters of an electronic component. The sub-surface layer plays an important

role, which in high-purity semiconductor devices could become significant due to miniaturization. The effects of the inductively coupled Ar plasma etching on the performance of (111) face CdZnTe detector were investigated by B. Song [15], who proposed and analyzed the influence of different solutions for etching. The proposed method could remove the damaged layer caused by mechanical polishing. Still, it also led to the surface composition deviating from the stoichiometric ratio and forming a Te-rich surface. They noticed that the Te-rich layer is a highly conductive region, which results in a large surface leakage current and affects the detection performance. Zhang et al. [16] proposed a new chemical mechanical polishing method (silica, hydrogen peroxide, and citric acid), effectively reducing surface roughness. Min et al. [17] analyzed the effect of hydrogen plasma on CdZnTe and showed that hydrogen plasma could fill the Cd vacancy defect on the surface and reduce the leakage current.

Photothermal spectroscopy was also used to investigate the surface treatment procedures and their influence on the surface quality. Zakrzewski et al. [18] applied piezoelectric phase spectra to determine both the energy gaps (E_g) and the thermal diffusivities of $Cd_xZn_{1-x}Se$ mixed crystals. The authors showed and interpreted the different amplitude and phase spectra characters depending on the surface preparation procedure for $Cd_{0.3}Zn_{0.7}Se$ and $Cd_{0.5}Zn_{0.5}Se$ samples. The mechanical (grounding, polishing) and chemical (etching) procedures of surface preparation and their impact on both the amplitude and phase of photothermal spectra were observed for $Zn_{1-x-y}Be_xMn_ySe$ compounds [19]. The surface defects in the samples' sub-surface damaged layer were also reported for ZnSe binary crystal [20].

There are many methods of surface quality testing, e.g., different imaging methods. Piezoelectric photothermal spectroscopy is a cheap and fast method. Other photothermal methods that use microphones or pyroelectrics as detectors are not sensitive (do not show) to effects related to surface states. This is an advantage and a disadvantage; in the case of thermal diffusivity studies in the frequency domain, there is no signal coming from the subsurface layer, and it is easier to interpret the obtained results (there are well-known models).

Still, more investigations and literature data on $Cd_{1-x}Be_xTe$ mixed crystals are needed. One article has been published so far [21], which determines thermal properties using the pyroelectric method in the frequency domain. The present work investigates the optical and thermal properties using piezoelectric photothermal spectroscopy. Adding beryllium to the CdTe matrix should give a similar effect in tuning the energy bandgap or lattice constant as in the case of zinc. This fact should be interesting for detecting purposes and producing better substrates for infrared sensors.

Here we report the first experimental data describing the properties of crystals grown in our laboratory. Piezoelectric photothermal spectroscopy was applied to characterize $Cd_{1-x}Be_xTe$ mixed crystals. This work aimed to investigate the optical properties of $Cd_{1-x}Be_xTe$ mixed crystals and the effect of surface treatment on the amplitude and phase spectra. On that basis, we aimed to find a procedure and the best solution for obtaining excellent surface quality among the samples.

2. Materials and Methods

Crystals investigated in this work were grown by using the vertical Bridgman technique. Before the growth process, starting mixtures were prepared from high-purity CdTe (6 N) and Be (99.9%) powders and put into a graphite crucible. The crucible was placed into a growth chamber, sealed, and evacuated. After evacuation, the external pressure of argon gas (around 90 atm.) was applied to reduce evaporation of the material during the growing. The temperature in the hot zone was set to 1600 K, with a stability better than 0.1 K. We used a 4 mm/h pulling rate to grow the crystal within two days. Typically, our crystals grown by the Bridgman high-temperature and high-pressure technique were 4–6 cm in length and 1 cm in diameter. We could cut 15–20 plates 1–1.5 mm thick from one crystal rod. Four specimens of beryllium content (in ingot) were measured for x = 0.01, 0.03,

0.05, and 0.1. Pure CdTe crystals were also measured for the same procedure of surface preparation. More details concerning the growth procedure can be found elsewhere [22].

The beryllium concentration in the samples was determined after crystal milling (in agate mortar) by applying the powder X-ray diffraction technique (Empyrean diffractometer, Malvern Panalytical) with a Cu anode used as a source of CuKα X-ray radiation (λ = 1.5406 Å). More details about the measurement were presented in previous work [23]. The diffraction data were fitted using the ReX v. 0.91 Rietveld analysis software. The following parameters were fitted: scale factor, 2-theta offset, background coefficients, and cell constant a for the CdTe structure. In this case, the beryllium in the CdTe was treated as a solid solution of the first type, and thus the main changes were mainly observed for the cell dimension. All U factors were isotropic and set to 0.5. The reflection shape was described by the pseudo-Voight function. For analysis, the necessary crystal structure file of CdTe (cif) was downloaded from the American Mineralogist Crystal Structure Database [24].

The XRD patterns of example CdBeTe mixed crystals (CdTe and $Cd_{0.9}Be_{0.1}Te$) powdered are presented in Figure 1a. Characteristic diffraction reflections from (111), (220), (311), (400), (331), (420), and (511) planes of the cubic phase (type of zinc blende structure) are visible on the patterns for both CdTe (black) and $Cd_{0.9}Be_{0.1}Te$ (red) samples. In the case of a mixed crystal, the diffraction peaks are shifted towards higher 2 θ in comparison to the position of these signals in the CdTe. Such behavior demonstrates the presence of mixed crystals, so the beryllium was successfully incorporated into the crystal lattice of CdTe. The absolute values of the lattice constant were calculated by the Rietveld method and the results that were obtained as the function of the composition are displayed in Figure 1b. Linear dependence of the lattice constant versus Be content confirms the composition of the grown crystals.

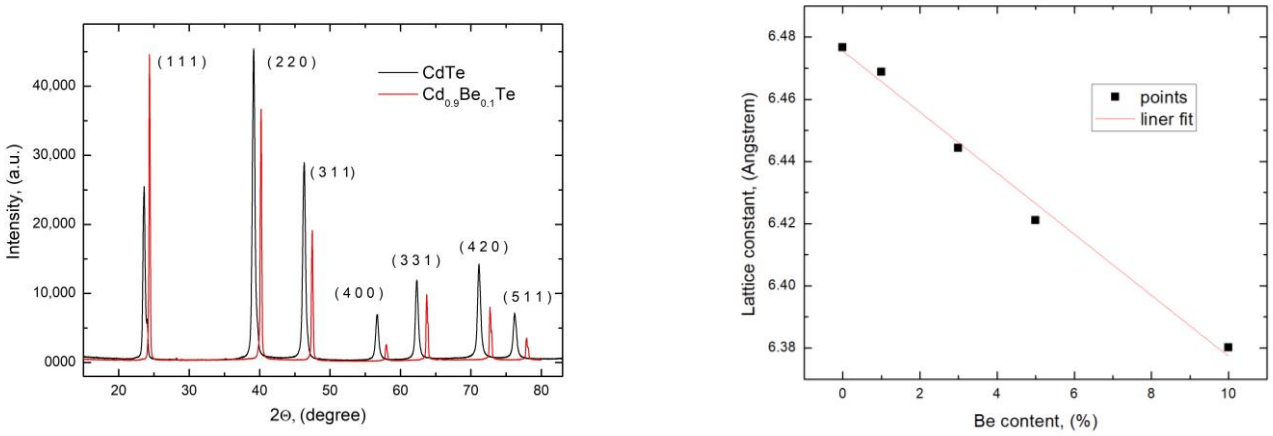

(**a**) (**b**)

Figure 1. The XRD patterns of CdTe (black) and $Cd_{0.9}Be_{0.1}Te$ (red) powders (**a**) and lattice constant versus beryllium concentration (**b**).

The cut samples were ground in a suspension of water and Al_2O_3 powder on flat glass parallel plates. The grain diameter of the grinding powder was approximately 10 µm. Then, the samples were polished with diamond paste on polishing discs until a mirror surface was obtained. The grain diameter in the polishing paste was between 0.1 and 1 µm.

The samples were subjected to two different etching processes. First, the samples were etched using a mixture containing 48% HF (hydrofluoric acid), 30% H_2O_2, and H_2O. Digestion took place at room temperature. The samples were subjected to photothermal tests. Then, the surfaces of the samples were ground and polished again to use a mixture of $K_2Cr_2O_7$, 96%H_2SO_4, and H_2O for etching. The etching took place at a temperature of about 80 °C. After etching, the samples were briefly immersed in a 50% NaOH solution, then rinsed in water, and finally in ethyl alcohol.

The typical experiment setups for piezoelectric detection, piezoelectric cell allowing front and rear detection, and lock-in detection were used [25]. A 150 W xenon lamp was used as the light source. The beam passed through a computer-controlled spectrometer; 90% of the beam fell on the photothermal cell and 10% on the photodiode, whose task was to monitor the light intensity. Cell and photodiode signals were measured by two lock-in Stanford SR 510 units. In piezoelectric detection, there are two possible ways of mutual arrangement of the detector and the measured sample. The detector is located behind the illuminated sample in the more commonly used rear configuration. In the front configuration, the detector is placed on the illuminated surface. Depending on the configuration, different course amplitude and phase spectra are observed.

3. Results

3.1. Cut and Grounded Samples

First, cut and grounded samples were examined. Figure 2 presents the experimental amplitude (blue) and phase (green) spectra of $Cd_{0.97}Be_{0.03}Te$ in the rear configuration at the frequency modulation of 126 Hz. In both spectra, the theoretical simulations for the ideal sample are presented (in black). The different characters of both experimental and simulated spectra are visible. There are two additional maxima in the sub-bang gap region for the amplitude and the significant change (at the energy of E = 1.46 eV) of the phase in the same area. The amplitude signal in the above bandgap area is increasing in comparing stable values in simulated amplitude spectra. Similar behavior was previously observed for $Zn_{1-x-y}Be_xMn_ySe$ compounds [19]. It was associated and interpreted as coming from the defects located on the surface of the sample and strictly connected with the method of surface preparation.

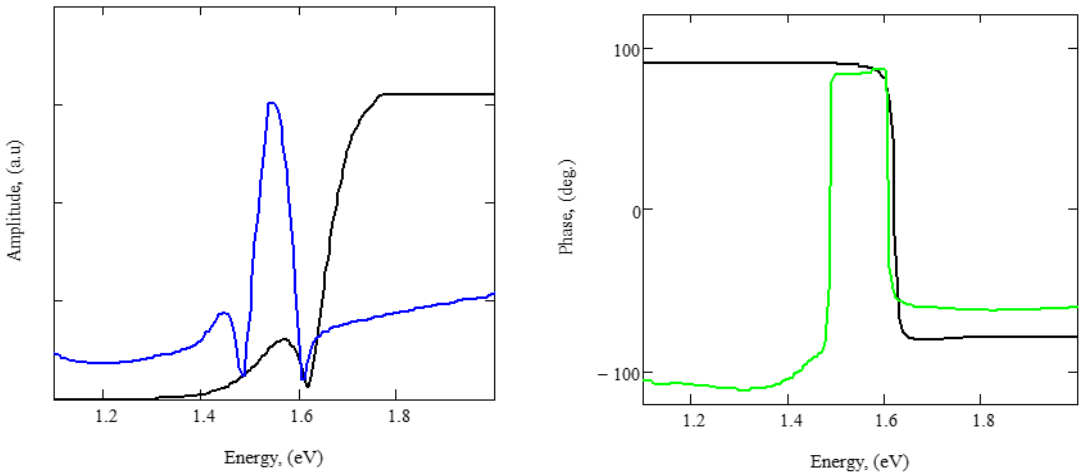

Figure 2. (**a**) Experimental amplitude (blue) and (**b**) phase (green) spectra of $Cd_{0.95}Be_{0.05}Te$ in the rear configuration at the frequency modulation of 126 Hz. The solid black lines simulate the ideal crystal's theoretical amplitude and phase spectra.

Figure 3 presents amplitude (a, b) and phase (c, d) spectra for $Cd_{0.99}Be_{0.01}Te$ grounded mixed crystals for different frequencies of modulation frequency and the rear (a, c) and front (b, d) configurations. In this case, the character of amplitude and spectra deviates from the theoretical predictions. For the lowest frequency (12 Hz), the additional maximum visible for higher frequencies is not visible. The higher the frequency, the higher the intensity of the maximum below the energy gap will be compared to the area above the energy gap: as the modulation frequency increases, the thermal diffusion length decreases, and the signal is generated from a smaller thickness. For low frequencies, the signal comes from a large sample thickness, and the signal from the surface is not dominant. It is worth noting that

regardless of the frequency, the points of inflection of the curves are observed in the phase spectra for the same energies.

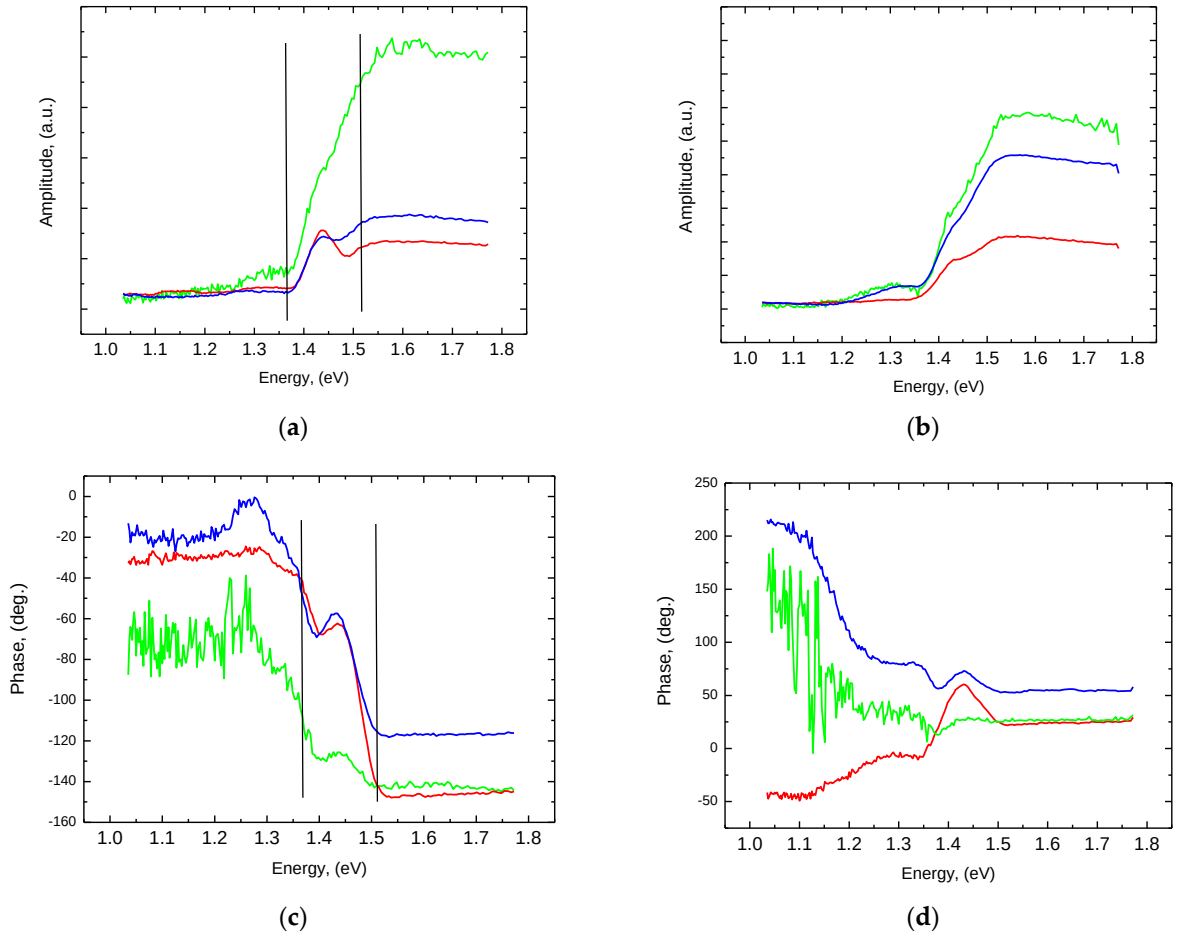

Figure 3. Amplitude (**a**,**b**) and phase (**c**,**d**) spectra for $Cd_{0.99}Be_{0.01}Te$ grounded mixed crystal for different frequencies of modulation frequency for the rear (**a**,**c**) and front (**b**,**d**) configurations at 12 Hz (blue lines), 76 Hz (green lines), and 126 Hz (red lines).

The different amplitude and phase spectra characters were observed for the $Cd_{0.9}Be_{0.1}Te$ mixed crystal. Figure 4 presents amplitude (a) and phase (b) spectra for this sample.

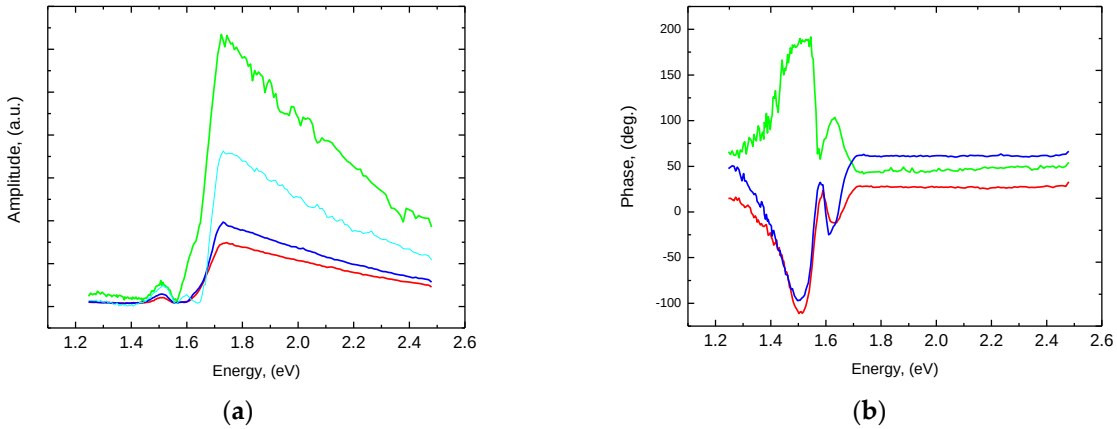

Figure 4. Amplitude (**a**) and phase (**b**) spectra for $Cd_{0.9}Be_{0.1}Te$ grounded mixed crystal for different frequencies of modulation frequency for the front configuration at 12 Hz (blue lines), 36 Hz (cyan line), 76 Hz (green lines), and 126 Hz (red lines).

Two maxima are observed for this sample in the amplitude spectra of E_1 = 1.51 eV and E_2 = 1.59 eV. The first one is present for all the frequencies, and its intensity is not changed compared to the intensity of the signal in the region above the energy gap. The behavior of the second maximum is similar to the one observed in the previous sample. A probable cause is that the thickness of the damaged layers on both surfaces is different. In the phase spectra, one must analyze the maxima and bending points to identify the localization of defects and their energetic positions.

Beryllium and defects related to its presence in the subsurface layer are undoubtedly responsible for changes in spectra and the formation of additional peaks. A strong correlation between surface preparation for $Zn_{1-x-y}Be_xMg_ySe$ [26] was previously observed, but no explanation has yet been found for the mechanisms of the formation of defects on the surface; research is ongoing to clarify their nature.

A decrease in amplitude spectra in the region above E_g (not a constant signal as in theory) was observed by Kuwahata et al. [27] in studies of implanted Si + ions in InP. According to them, silicon ions are responsible for defects in the crystal lattice and suppress the propagation of an elastic wave, which causes a decrease in the amplitude above the energy gap region. This is related to an increase in the number of free carriers in the conduction band states in the annealed samples. When these states are filled, photons of the energy close to the energy gap are not absorbed, and the photothermal signal is not generated.

A similar effect was also reported by Matsumori et al. [28] in studies of the impact of damage caused by ion implantation in Si. The photothermal signal was sensitive to the size and structure of damage in the layer with implanted ions. The authors attributed the signal reduction below the energy gap of the surface quality and the defects present on it. Its damage suppresses the generation of elastic waves. The authors came to conclusions that can also be drawn from the current research: the increased number of defects on the surface causes a more significant generation of thermal energy in the sub-bandgap region and the opposite effect for the area above the gap. Here, the thermoelastic waves are suppressed.

3.2. The Change of the Energy Gap with the Be Content

The series of $Cd_{1-x}Be_xTe$ samples was measured to obtain the energy gap values' dependence on the beryllium content described by the composition parameter (x). The amplitude and phase spectra were measured for the samples: x = 0.01, 0.03, 0.5, 0.1. A pure CdTe sample was also measured and subjected to the same surface treatment procedure. The amplitude and phase spectra for the modulation frequency of 126 Hz are presented in Figure 5. There was an increase in the value of E_g with the rise of beryllium content (clearly visible). Calculating the energy gap value from the phase and amplitude spectra was possible. The values could be estimated directly from the spectra or calculated as a parameter from the theory.

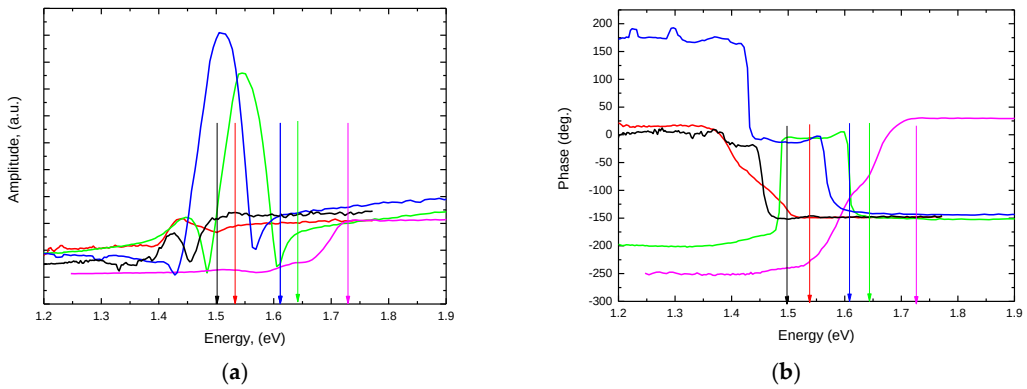

Figure 5. Amplitude (**a**) and phase (**b**) spectra of $Cd_{1-x}Be_xTe$ for different beryllium content. Black line: x = 0, red: x = 0.01, blue: x = 0.03, green: x = 0.05, magenta: x = 0.1. The color arrows indicate the values of energy gaps.

The phase spectra course may differ for different samples and frequencies. Still, the most important are the changes (inflection points) at which these changes occur: they indicate additional photothermal signal sources and the energetic position of the defects on the surface.

The obtained values of energy gaps are presented in Table 1.

Table 1. The experimental values of E_g for $Cd_{1-x}Be_xTe$.

x	Energy Gap (E_g), eV
0	1.49 eV
0.01	1.53 eV
0.03	1.61 eV
0.05	1.64 eV
0.1	1.72 eV

3.3. Etched Samples

One of the sample preparation goals was to obtain a perfect-quality surface. First, the polished samples were subjected to etching using a mixture containing 48% HF (hydrofluoric acid), 30% H_2O_2, and H_2O. This procedure caused the photothermal signal to be wholly quenched for mixed samples, making it impossible to measure the spectra. A possible explanation for this will be discussed later in this article. Therefore, it was decided to grind the samples again and further etch them in a new solution. The surfaces of the specimens were ground and polished to use a mixture of $K_2Cr_2O_7$, 96% H_2SO_4, and H_2O for the etching.

Figure 6 compares the amplitude spectra for the ground and etched $Cd_{0.95}Be_{0.05}Te$ sample.

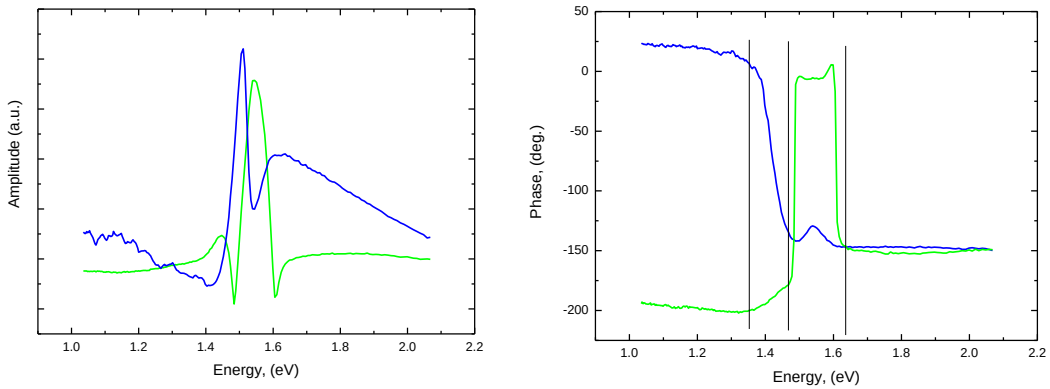

(**a**) (**b**)

Figure 6. Amplitude (**a**) and phase (**b**) spectra for the ground (green lines) and etched (blue lines) $Cd_{0.95}Be_{0.05}Te$ sample at 126 Hz of modulation frequency.

The expectation was to obtain the spectra close in shape to the ideal crystal (black in Figure 2). The applied method of etching did not improve the surfaces of the sample. In the amplitude spectrum, an additional maximum still exists below the energy gap, which is not expected for an ideal sample. Although the phase has a different shape, it is worth noting that phase changes take place at the same energy values (indicated in the figure with vertical lines). This proves that the defects on the surface were present at a different depth of the damaged layer (by etching) or that additional effects had been achieved, e.g., with phenomena associated with the carriers. The same changes in phase are manifested differently in amplitude; with different maximums, it is also worth emphasizing that piezoelectric spectroscopy allows for studying the differences on both surfaces of the sample prepared with the same treatment procedure.

Figures 7 and 8 present the experimental spectra of the amplitude and phase of $Cd_{0.95}Be_{0.05}Te$ after the etching process was obtained for the illumination of different sur-

faces of the sample. The sample was measured in rear and front configurations. The surfaces of the samples were assigned numbers 1 and 2 and then measured after illumination of surface 1, then 2. The aim was to examine and compare the surfaces after an identical treatment procedure.

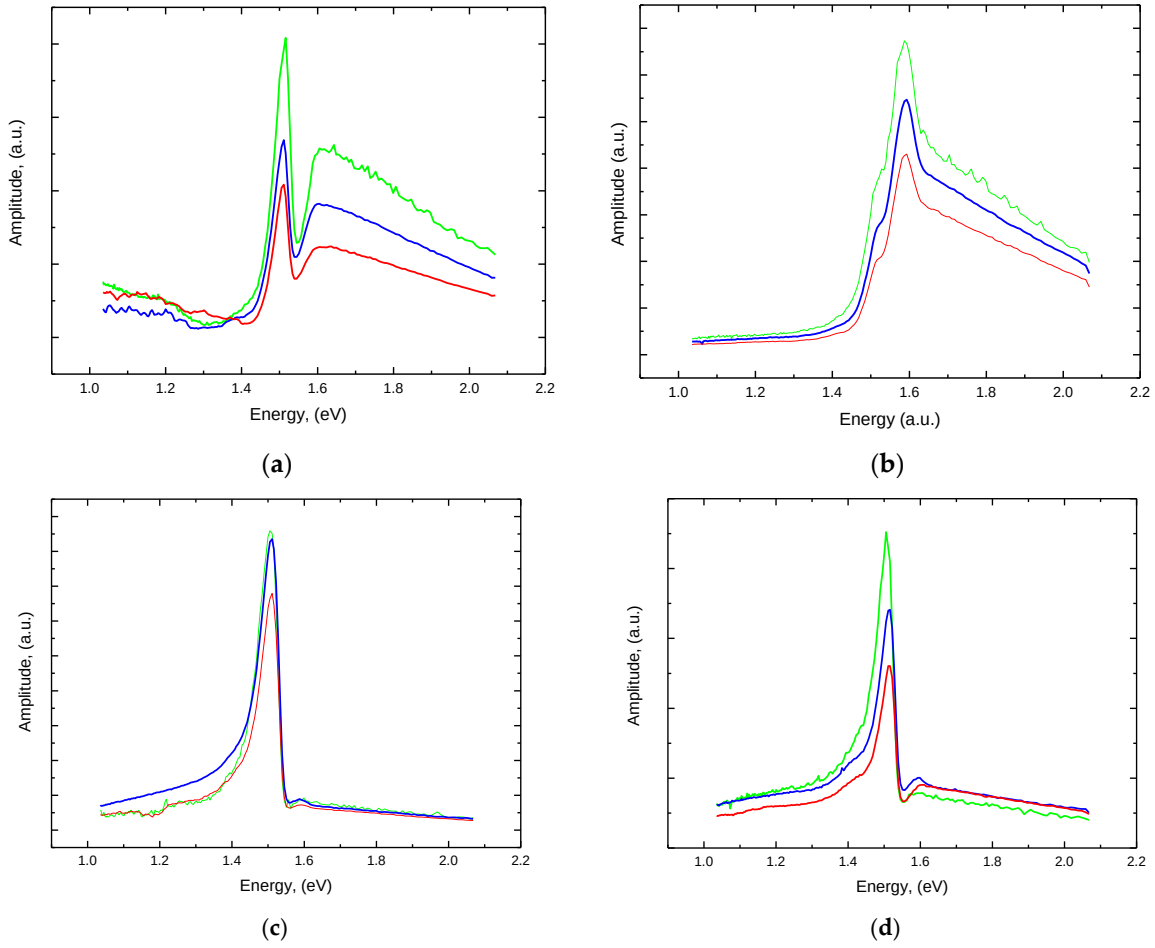

Figure 7. Amplitude spectra of $Cd_{0.95}Be_{0.05}Te$ for front and rear detection and illumination of different surfaces at 12 Hz (blue lines), 76 Hz (green lines), and 126 Hz (red lines). (**a**) Surface 1 illuminated, rear detection. (**b**) Surface 1 illuminated, front detection. (**c**) Surface 2 illuminated, rear detection. (**d**) Surface 2 illuminated, front detection.

Complementarity, especially in the amplitude spectra, is evident. Whether rear or front detection is considered, the strong maximum associated with the surface defect is observed for the illumination at surface 2. Its intensity is much higher in comparison to the above bandgap region, which indicates that etching negatively affects the quality of the surfaces, and the defects strengthen the photothermal signal. In the case of illumination of surface 1, the amplitude spectra have a similar character with a smaller maximum in the sub-bandgap region. The maximum has a higher intensity for rear detection and is associated with subtracting the piston and drum effects.

The phase spectra for the illumination of surface 2 show the changes at the same energy values despite the curves' different characters. The more significant differences are observed for phase spectra for front detection and the illumination at surface 1. It should be emphasized that both phase and amplitude must be analyzed to interpret piezoelectric spectra correctly.

The same change of character was also observed for the rest of the samples, which proved that the chosen etching procedure introduced additional defects on the surfaces of the samples.

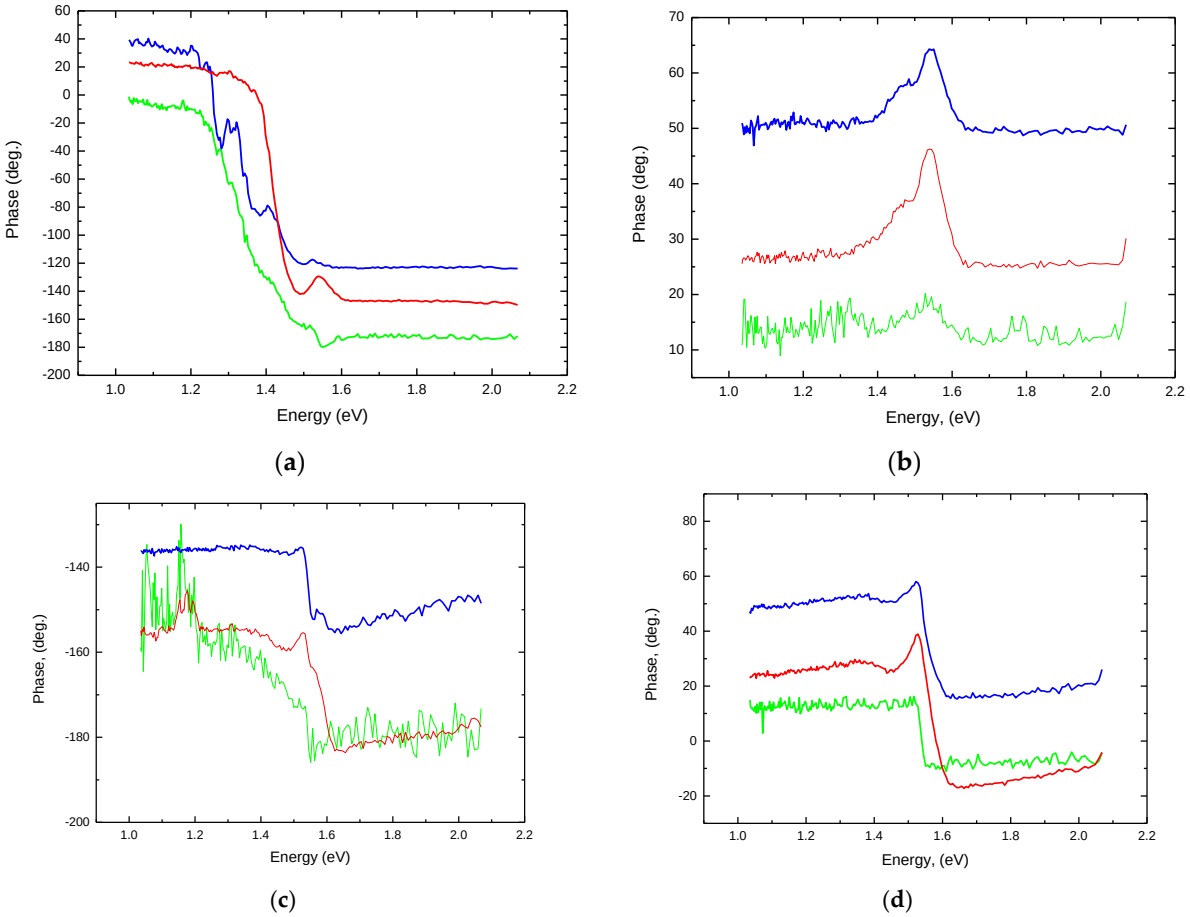

Figure 8. Phase spectra of $Cd_{0.95}Be_{0.05}Te$ for front and rear detection and illumination of different surfaces at 12 Hz (blue lines), 76 Hz (green lines), and 126 Hz (red lines). (**a**) Surface 1 illuminated, rear detection. (**b**) Surface 1 illuminated, front detection. (**c**) Surface 2 illuminated, rear detection. (**d**) Surface 2 illuminated, front detection.

4. Discussion

The amplitude and phase spectra courses for the ideal semiconductor are known [25]. To measure against them, the temperature distribution in the tested sample and the waveforms for the absorption coefficient below and above the band gap were required. The expression for the absorption coefficient is one of the parameters of the temperature distribution. The expression for the phase and amplitude of the photothermal signal depends on this distribution. Details are presented in prior work [25].

The changes observed in the experimental spectra were interpreted as originating from defects located on the surface of the samples, as they were observed to be strongly dependent on the method of surface preparation. To simulate the changes, it was assumed that the defects could be simulated in temperature distributions with Gauss-shaped expressions. In the simulations, parameters such as energy, thermal diffusivity, and thermal conductivity were determined, and their courses were compared with the obtained experimental spectra.

The modified Blonskij's model [26,29,30] was applied to interpret the obtained spectra. The heat conduction equation describes the sample's temperature distribution as previously described [30]. The modified model considers a damaged subsurface layer on both surfaces of the sample with significantly different thermal parameters from the main part of the sample. The absorption coefficient due to the presence of the defects has the Gaussian character.

$$\beta = A_d \cdot exp\left(\frac{E - E_d}{\beta_1}\right)^2 \quad (1)$$

where E_d is the value of the energy of the defect, β_1 is the parameter describing the width of Gaussian shape maximum, and A_d is the amplitude of the maximum.

The defect is located at the surfaces of the sample, and its nature can be associated with the quality of the surface after the preparation process (grounding, polishing, etching). For the energy E_d of radiation, the layer strongly absorbs, while the volume of the sample is transparent. The temperature distribution in the sample is the sum of temperatures generated on the surface and the volume of the sample:

$$T'(x) = T(x) + T_1^d(x) + T_2^d \tag{2}$$

The piezoelectric signal is given by the expression [24]

$$V \sim \left(\frac{1}{l} \int_{-l/2}^{l/2} T'(x)dx \pm \frac{6}{l^2} \int_{-l/2}^{l/2} T'(x)xdx \right) \tag{3}$$

Two terms in the expression represent piston and drum effects [26]; they add up in the case of front detection and subtract in the case of rear mode.

Assuming the proper expressions for the absorption coefficient in the direct bandgap semiconductors (Urbach tail thermal broadening and absorption connected with the band-to-band electron transitions) [26], one can simulate the amplitude and phase spectra for the semiconducting sample with the presence of the defects localized on the subsurface damaged layer.

The nature of the amplitude and phase spectra is influenced by thermal bulk and layer parameters, the most important of which are thermal diffusivities, energy gaps, and the thicknesses of the sample and the near-surface layer. These basic parameters characterizing the material were used to simulate both amplitude and phase spectra.

Figure 9 presents amplitude (a) and phase (b) spectra of ground $Cd_{0.95}Be_{0.05}Te$ mixed crystal. Experimental data are shown together with simulations according to the above-given model. The simulation was performed for the presence of two defects with the location E_{d1} = 1.51 eV and E_{d2} = 1.55 eV, thermal diffusivity of 0.05 cm^2/s, thermal conductivity of 0.07 W/(cm·K) for the sample, and conductivity of the layer, ten times smaller than the bulk: A_{d1} = 15 cm^{-1}, A_{d2} = 7 cm^{-1}, β_1 = 0.2 cm^{-1}, β_2 = 0.06 cm^{-1}. The thickness of the defective layer was 0.01 mm. The simulations qualitatively confirm the presence of defects on the surface, but they are not entirely consistent with the experiment data.

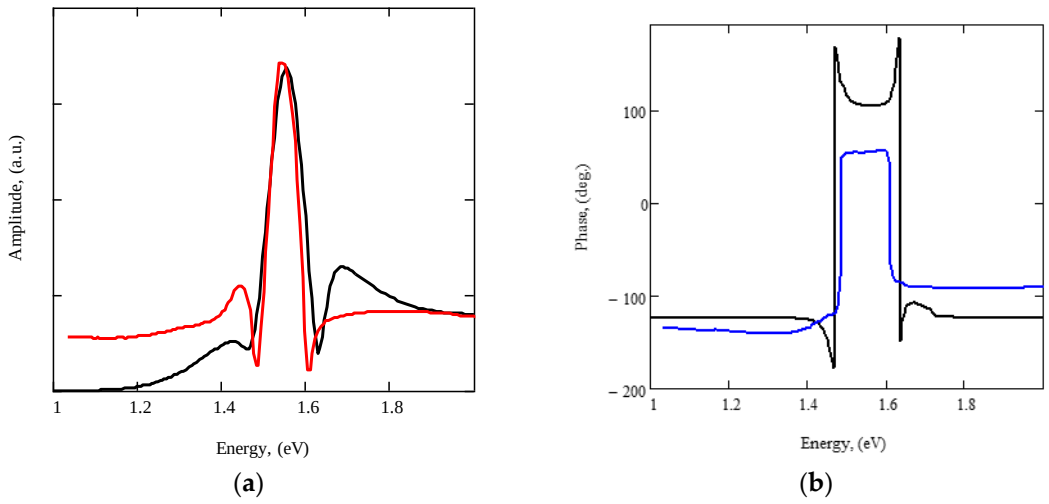

Figure 9. Amplitude (**a**) and phase (**b**) spectra of the ground $Cd_{0.95}Be_{0.05}Te$ mixed crystal for 126 Hz modulation frequency. Simulated spectra are presented by black lines, experimental amplitude by red lines, and experimental phase by blue lines.

Figure 10 presents amplitude (a) and phase (b) spectra of etched $Cd_{0.95}Be_{0.05}Te$ mixed crystal. Experimental data are shown together with simulations. The simulation was performed for the presence of two defects with a location different than the previous case: E_{d1} = 1.6 eV and E_{d2} = 1.62 eV, thermal diffusivity of 0.05 cm^2/s, thermal conductivity of 0.07 W/(cm·K) for the sample, and conductivity of the layer, 12 times smaller than the bulk: A_{d1} = 110 cm^{-1}, A_{d2} = 80 cm^{-1}, β_1 = 0.045 cm^{-1}, β_2 = 0.06 cm^{-1}. The thickness of the defective layer was 0.001 mm, ten times smaller than in the previous case. In this case, lower compatibility in experiment and simulation was achieved.

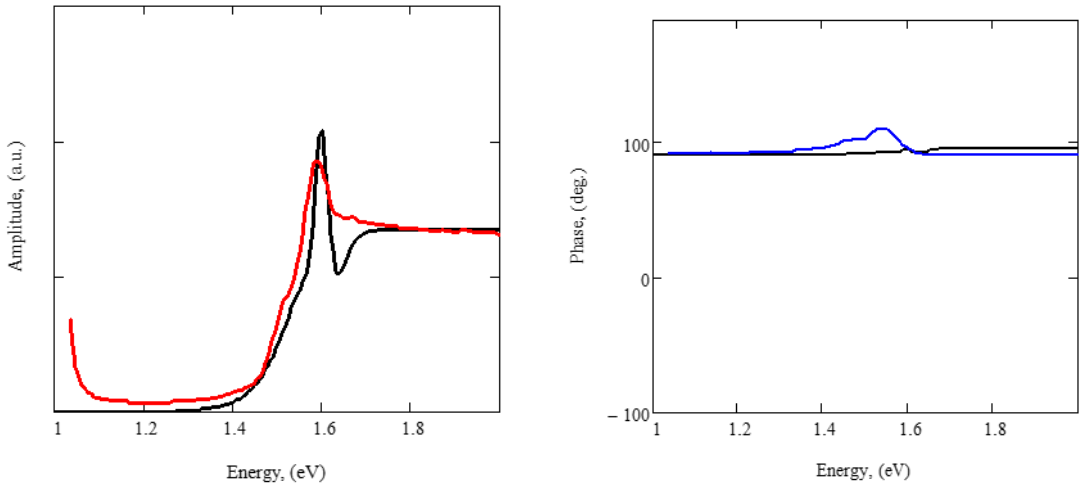

Figure 10. Amplitude (**a**) and phase (**b**) spectra of the etched $Cd_{0.95}Be_{0.05}Te$ mixed crystal for 126 Hz modulation frequency. Simulated spectra are presented by black lines, experimental amplitude by red lines, and experimental phase by blue lines.

The applied theory assumes the generation of a photothermal signal only due to the thermoelastic effect. As shown before, the fall of the signal above the gap may be due to free carrier contribution. Their participation should also be considered when generating the signal in the defective subsurface layer. This assumption can be supported by the most recent results obtained by Aleksić et al. [31]. In their article, the dependence of the photoacoustic signal on the frequency of the excitation beam was used to analyze the influence of thin transparent foil on the thermal and elastic properties of a two-layer sample consisting of a silicon substrate and a thin TiO_2 foil. A thin layer can significantly affect the substrate's thermal state and increase the sample's bending. This is related to a slight change in the number of photogenerated carriers in the transparent layer, which strongly influences the temperature differences between the illuminated and non-illuminated sides of the sample [31]. The influence of the carriers in the defective layer probably extinguished the signal for the first sample etching procedure.

5. Conclusions

Using piezoelectric photothermal spectroscopy, a new $Cd_{1-x}Be_xTe$ material was investigated, and its basic optical parameters were determined (E_g primary and thermal diffusivity). The influence of the sample preparation method on the amplitude and phase of the photothermal signal was observed and interpreted. High-quality sample surfaces have yet to be achieved, and further work on surface treatment procedures is needed. Further research and development of an appropriate etching method are required to obtain a defect-free surface of the samples. The next step will be to measure the different etching mixtures and etching times. The extinction of the signal-etching procedure may have been caused by excessive etching time. Despite not achieving good surface quality, piezoelectric spectroscopy is a sensitive method and can help choose the appropriate surface treatment method to obtain the desired quality.

In this paper, we presented a preliminary interpretation of our experimental data using the modified Blonskij model. As not all courses of the amplitude and phase could be interpreted with the proposed theory, it is necessary to expand it. We have shown that considering only the thermoelastic effect for analyzing and simulating experimental spectra cannot fully reproduce them. Effects related to carriers should also be considered in the interpretation, both in terms of nonradiative bulk recombination of carriers that diffuse in the crystal and the nonradiative surface recombination of carriers.

Author Contributions: Methodology, D.M.K.; Investigation, J.Z., K.S., M.B., A.M., A.A. and D.M.K.; Writing—original draft, J.Z. All authors have read and agreed to the published version of the manuscript.

Funding: This research was funded by Emerging Fields Team IDUB of Nicolaus Copernicus University—Material Science and Technology, 2023–2026.

Institutional Review Board Statement: Not applicable.

Data Availability Statement: The data presented in this study are available on request from the corresponding author.

Conflicts of Interest: The authors declare no conflict of interest.

References

1. Schlesinger, T.; Toney, J.; Yoon, H.; Lee, E.; Brunett, B.A.; Franks, L.; James, R.B. Cadmium zinc telluride and its use as a nuclear radiation detector material. *Mater. Sci. Eng.* **2001**, *32*, 103–189. [CrossRef]
2. Choi, H.; Jeong, M.; Kim, H.S.; Kim, Y.S.; Ha, J.H.; Chai, J.-S. Growth and Fabrication Method of CdTe and Its Performance As a Radiation Detector. *J. Korean Phys. Soc.* **2015**, *66*, 27–30. [CrossRef]
3. Szeles, C.; Cameron, S.E.; Ndap, J.O.; Chalmers, W. Advances in the High-pressure Crystal Growth Technology of Semi-insulating CdZnTe for Radiation Detector Applications. *IEEE Trans. Nucl. Sci.* **2002**, *49*, 2424–2428. [CrossRef]
4. Del Sordo, S.; Abbene, L.; Caroli, E.; Mancini, A.M.; Zappettini, A.; Ubertini, P. Progress in the Development of CdTe and CdZnTe Semiconductor Radiation Detectors for Astrophysical and Medical Applications. *Sensors* **2009**, *9*, 3491–3526. [CrossRef]
5. Partovi, A.; Millerd, J.; Garmire, E.M.; Ziari, M.; Steier, W.H.; Trivedi, S.B.; Klein, M.B. Photorefractivity at 1.5 μm in CdTe:V. *Appl. Phys. Lett.* **1990**, *57*, 846–848. [CrossRef]
6. Sen, S.; Liang, C.S.; Rhiger, D.R.; Stannard, J.E.; Arlinghaus, H.F. Reduction of CdZnTe substrate defects and relation to epitaxial HgCdTe quality. *J. Electron. Mater.* **1996**, *25*, 1188–1195. [CrossRef]
7. Szeles, C.; Soldner, S.A.; Vydrin, S.; Graves, J.; Bale, D.S. CdZnTe Semiconductor Detectors for Spectroscopic X-ray Imaging. *IEEE Trans. Nucl. Sci.* **2008**, *55*, 572–582. [CrossRef]
8. Zhoua, C.; Yang, J.; Yu, H.; Xu, C.; Shi, Y. Study of the extended defects in CdZnTe crystal. *J. Cryst. Growth* **2020**, *544*, 125725.
9. Gu, J.; Shen, Y.; Wen, D.; Huang, J.; Lai, J.; Gu, F.; Cao, M.; Wang, L.; Min, J. Marked effects of Al-rich AlN transition layers on the performance of CdZnTe films for solar-blind photodetector. *Vacuum* **2021**, *193*, 110539. [CrossRef]
10. Li, Y.; Zha, G.; Guo, Y.; Xi, S.; Xu, L.; Yu, H.; Jie, W. Effects of deep-level traps on the transport properties of high-flux X-ray CdZnTe detectors. *Mater. Sci. Semicond. Process.* **2021**, *133*, 105974.
11. Aqariden, F.; Tari, S.; Nissanka, K.; Li, J.; Kioussis, N.; Pimpinella, R.E.; Dobrowolska, M. Influence of surface polishing on the structural and electronic properties of CdZnTe surfaces. *J. Electron. Mater.* **2012**, *41*, 2893–2898. [CrossRef]
12. Zheng, Q.; Dierre, F.; Crocco, J.; Carcelen, V.; Dieguez, E. Influence of surface preparation on CdZnTe nuclear radiation detectors. *Appl. Surf. Sci.* **2011**, *257*, 742–8746. [CrossRef]
13. Tari, S.; Aqariden, F.; Chang, Y.; Grein, C.; Li, J.; Kioussis, N. Impact of surface treatment on the structural and electronic properties of polished CdZnTe surfaces for radiation detectors. *J. Electron. Mater.* **2013**, *42*, 3252–3258. [CrossRef]
14. Hossain, A.; Bolotnikov, A.E.; Camarda, G.S.; Cui, Y.; Jones, D.; Hall, J.; Kim, K.H.; Mwathi, J.; Tong, X.; Yang, G.; et al. Novel approach to surface processing for improving the efficiency of CdZnTe detectors. *J. Electron. Mater.* **2014**, *43*, 2771–2777. [CrossRef]
15. Song, B.; Zhang, J.; Liang, X.; Zhao, S.; Min, J.; Shi, H.; Lai, J.; Wang, L. Effects of the inductively coupled Ar plasma etching on the performance of (111) face CdZnTe detector. *Mater. Sci. Semicond. Process.* **2020**, *109*, 104929. [CrossRef]
16. Zhang, Z.; Wang, B.; Zhou, P.; Kang, R.; Zhang, B.; Guo, D. A novel approach of chemical mechanical polishing for cadmium zinc telluride wafers. *Sci. Rep.* **2016**, *6*, 26891. [CrossRef]
17. Min, J.; Li, H.; Wang, L.; Zhang, J.; Liang, X.; Liu, W.; Sun, X.; Wang, D.; Yuan, Z.; Wei, G.; et al. The effect of hydrogen plasma treatment on the Au–CdZnTe interface. *Surf. Coat. Technol.* **2013**, *228*, 97–100. [CrossRef]
18. Zakrzewski, J.; Maliński b, M.; Bachiri, A.; Strzałkowski, K. Photothermal determination of the optical and thermal parameters of $Cd_xZn_{1-x}Se$ mixed crystals. *Mater. Sci. Eng. B* **2021**, *271*, 115305. [CrossRef]
19. Maliński, M.; Zakrzewski, J.; Strzałkowski, K. Numerical Analysis of Piezoelectric Spectra of $Zn_{1-x-y}Be_xMn_ySe$ Mixed Crystals. *Int. J. Thermophys.* **2007**, *28*, 229–316. [CrossRef]

20. Zakrzewski, J.; Maliński, M.; Strzałkowski, K. Influence of the Surface Mechanical Treatment on the Photothermal Piezoelectric Spectra of ZnSe Crystals. *Int. J. Thermophys.* **2012**, *33*, 1228–1238. [CrossRef]
21. Singh, D.; Strzałkowski, K.; Abouais, A.; Alaoui-Belghiti, A. Study of the Thermal Properties and Lattice Disorder Effects in CdTe–Based Crystals: CdBeTe, CdMnTe, and CdZnTe. *Crystals* **2022**, *12*, 1555. [CrossRef]
22. Firszt, F.; Łegowski, S.; Meczynska, H.; Szatkowski, J.; Paszkowicz, W.; Godwod, K. Growth, and characterization of $Zn_{1-x}Be_xSe$ mixed crystals. *J. Cryst. Growth* **1998**, *184–185*, 1335. [CrossRef]
23. Gorgol, M.; Zaleski, R.; Kierys, A.; Kamiński, D.; Strzałkowski, K.; Fedus, K. Positron lifetime spectroscopy of defect structures in $Cd_{1-x}Zn_xTe$ mixed crystals grown by vertical Bridgman–Stockbarger method. *Acta Cryst.* **2021**, *B77*, 515–525.
24. Downs, R.T.; Hall-Wallace, M. The American Mineralogist Crystal Structure Database. *Am. Miner.* **2003**, *88*, 247–250.
25. Zakrzewski, J.; Maliński, M.; Strzałkowski, K.; Firszt, F.; Łęgowski, S.; Męczyńska, H. Influence of Surface Preparation for Different Groups of A2B6 Mixed Crystals. *Int. J. Thermophys.* **2010**, *31*, 208–217. [CrossRef]
26. Maliński, M.; Zakrzewski, J.; Strzałkowski, K.; Łęgowski, S.; Firszt, F.; Męczyńska, H. Piezoelectric photoacoustic spectroscopy of surface states of $Zn_{1-x-y}Be_xMg_ySe$ mixed crystals. *Surf. Sci.* **2009**, *603*, 131–137. [CrossRef]
27. Kuwahata, H.; Muto, N.; Uehara, F.; Matsumori, T. Comparison of Annealing Behavior in Photoacoustic Signal Intensity of Si+ Implanted InP by Microphone an Piezoelectric Transducer Method. *AIP Conf. Proc.* **1999**, *463*, 250–252.
28. Matsumori, T.; Uchida, M.; Yoshinaga, H.; Kawai, J.; Izumi, T.; Uehara, F. Photoacoustic Characterization Of Ion-Implanation Damage in Silicon. In *Phoacoustic and Photothermal Phenomena III*; Springer Series in Optical Sciences; Springer: Berlin, Germany, 1992; Volume 69, pp. 357–359.
29. Blonskij, I.; Tkhoryk, V.; Shendeleva, M. Thermal diffusivity of solids determination by photoacoustic piezoelectric technique. *J. Appl. Phys.* **1996**, *79*, 3512–3516. [CrossRef]
30. Zakrzewski, J.; Maliński, M.; Chrobak, Ł.; Pawlak, M. Comparison of Theoretical Basics of Microphone and Piezoelectric Photothermal Spectroscopy of Semiconductors. *Int. J. Thermophys.* **2017**, *38*, 2. [CrossRef]
31. Aleksić, S.M.; Markushev, D.K.; Markushev, D.D.; Pantić, D.S.; Lukić, D.V.; Popović, M.N.; Galović, S.P. Photoacoustic Analysis of Illuminated Si-TiO_2 Sample Bending Along the Heat-Flow Axes. *Silicon* **2022**, *14*, 9853–9861. [CrossRef]